

# A 1.4-m $\Omega$ -Sensitivity 94-dB Dynamic-Range Electrical Impedance Tomography SoC and 48-Channel Hub-SoC for 3-D Lung Ventilation Monitoring System

Minseo Kim, *Student Member, IEEE*, Jaeeun Jang, *Student Member, IEEE*, Hyunki Kim, *Student Member, IEEE*, Jihee Lee, *Student Member, IEEE*, Jaehyuck Lee, *Student Member, IEEE*, Jiwon Lee, *Student Member, IEEE*, Kyoung-Rog Lee, *Student Member, IEEE*, Kwantae Kim, *Student Member, IEEE*, Yongsu Lee, *Member, IEEE*, Kyuho Jason Lee, *Student Member, IEEE*, and Hoi-Jun Yoo, *Fellow, IEEE*

**Abstract**—A wearable electrical impedance tomography (EIT) system is proposed for the portable real-time 3-D lung ventilation monitoring. It consists of two types of SoCs, active electrode (AE)-SoC and Hub-SoC, mounted on wearable belts. The 48-channel AE-SoCs are integrated on flexible printed circuit board belt, and Hub-SoC is integrated in the hub module which performs data gathering and wireless communication between an external imaging device. To get high accuracy under the variation of conductivity, the dual-mode current stimulator provides the optimal frequency for time difference-EIT and frequency difference-EIT with simultaneous 4 k–128 kHz impedance sensing. A wide dynamic range instruments amplifier is proposed to provide 94 dB of wide dynamic range impedance sensing. In addition, the 48-channel AE system with the dedicated communication and calibration is implemented to achieve 1.4-m $\Omega$  sensitivity of impedance difference in the *in vivo* environment. The AE-Hub-SoCs occupy 3.2 and 1.3 mm<sup>2</sup> in 65-nm CMOS technology and consume 124  $\mu$ W and 1.1 mW with 1.2 V supply, respectively. As a result, EIT images are reconstructed with 90% of accuracy, and up to 10 frames/s real-time 3-D lung images are successfully displayed.

**Index Terms**—3-D-imaging, active electrode (AE), electrical impedance tomography (EIT), impedance spectroscopy, lung ventilation monitoring, real-time imaging, wide dynamic range.

## I. INTRODUCTION

Mechanical lung ventilation is important to the patients with acute lung injury in intensive care unit. However, inaccurate control of mechanical ventilation can cause ventilator-induced lung injury, which brings several complications. In fact, more than 50 million patients are mechanically ventilated and 5.7 million patients develop acute lung injury every year [1]–[2]. Among them, 2.2 million people lose their lives due to wrong ventilation [3]–[4]. Both of excessive and deficient ventilation can occur

Manuscript received May 14, 2017; revised August 28, 2017; accepted September 11, 2017. Date of publication October 3, 2017; date of current version October 23, 2017. This work was supported by the Institute for Information and Communications Technology Promotion (IITP) grant through the Korea Government (MSIT) (R7117-16-0169). This paper was approved by Guest Editor Peng Cong. (*Corresponding author: Minseo Kim*)

The authors are with the Korea Advanced Institute of Science and Technology, Daejeon 305-701, South Korea (e-mail: minseokim@kaist.ac.kr).

Color versions of one or more of the figures in this paper are available online at <http://ieeexplore.ieee.org>.

Digital Object Identifier 10.1109/JSSC.2017.2753234

over-distention or collapse of alveoli. Therefore, a careful compromise must be found between positive end-expiratory pressure (PEEP)-induced alveolar recruitment and the prevention of hyperinflation. In other words, there is a need for clinicians to optimize the ventilator settings, which are the volume and the pressure of air, to obtain the optimized PEEP for individual patients at the bedside [5]. However, finding and maintaining these crucial settings during therapy is challenging even for experienced clinicians because the optimal point varies by individuals [6]. To solve these problems, several methods to monitor lung ventilation continuously at bedside have been reported such as capnography or pulse oximeter. However, because these systems cannot provide regional information of lung and they suffer from their long latency, they provide inaccurate information to guide ventilation parameters in real-time. Another method called the chest X-ray computed tomography is widely used to provide images containing regional information of lung. This system has very high resolution, but it inevitably involves radiation and is not suitable for continuous monitoring. Therefore, a real-time monitoring system that provides regional information of ventilation and pulmonary circulation in the injured lungs is essential to set correct values of pressure and volume of the ventilator.

One of the promising technologies for lung ventilation monitoring is electrical impedance tomography (EIT). EIT is an imaging technique which estimates the electrical conductivity distribution within the interior of a body by using the actual impedance values that are measured on its surface [7]. EIT has been widely studied to measure the impedance distribution to monitor lung ventilation because it is the only real-time lung imaging method without large equipment [8]–[12]. However, previous EIT systems that only provided 2-D cross-sectional images with limited spatial information of the lung causes unneglectable volume detection error depending on the location of 2-D-EIT belt relative to the patient's lung, because 3-D information is reflected to the cross-sectional area of the 2-D plane in 2-D-EIT [13]. Therefore, a new 3-D-EIT system that is capable of real-time monitoring is required to achieve much accurate images. In spite of its importance, the 3-D-EIT has not been realized in lung monitoring because it has many

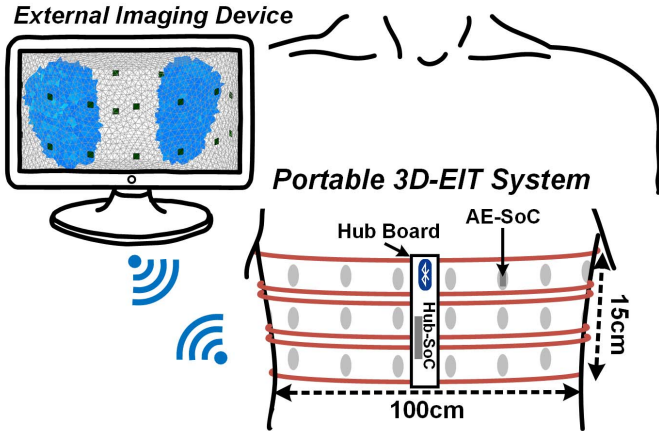


Fig. 1. Proposed wearable 3-D lung ventilation monitoring system.

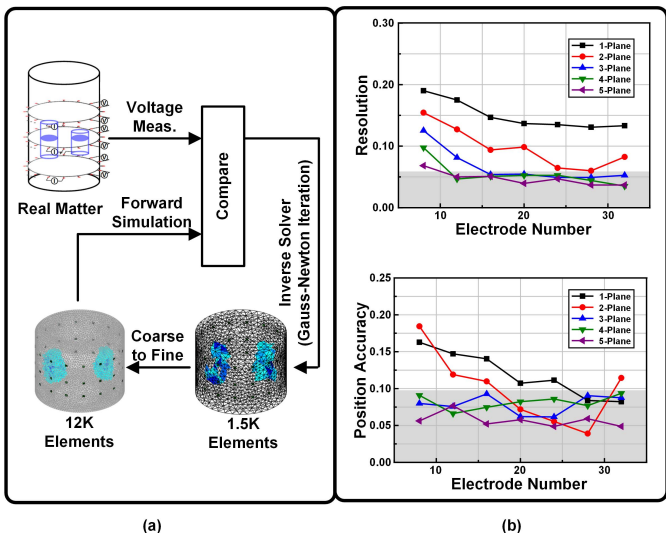


Fig. 2. (a) 3-D image reconstruction. (b) Image accuracy versus # of electrode and plane.

design challenges such as noises incurred by complicated wiring, long cable length, wide variation in electrode contact and signal, and large personal-to-person impedance variation.

In this paper, we present a wearable 3-D-EIT SoC for real-time lung ventilation monitoring with five features.

- 1) The active electrodes (AE) system to reduce coupling noise.
- 2) High output impedance current stimulator to inject stable current under wide variation of load condition.
- 3) Wide dynamic range front-end circuit to detect wide range of signal with high output impedance and common-mode rejection ratio (CMRR).
- 4) A new impedance spectroscopy to facilitate both time difference (TD)-EIT and frequency difference (FD)-EIT, and to find the optimal frequency for TD-EIT.
- 5) The 48 sensor-node calibration for robust operation.

The rest of the paper is organized as follows. Section II provides the proposed lung ventilation monitoring system. Section III introduces the implementation details of the EIT-SoC. Section IV shows the measurement results of both *in vitro* and *in vivo* tests including the performance summary. Finally, conclusions are drawn in Section V.

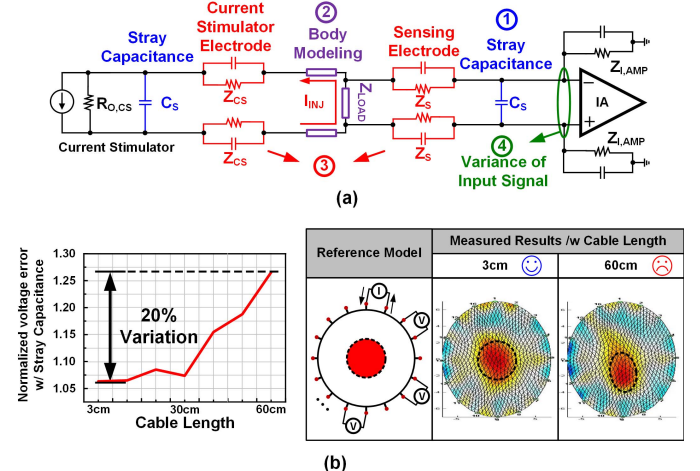


Fig. 3. (a) Error source of EIT measurement. (b) Stray capacitance effect.

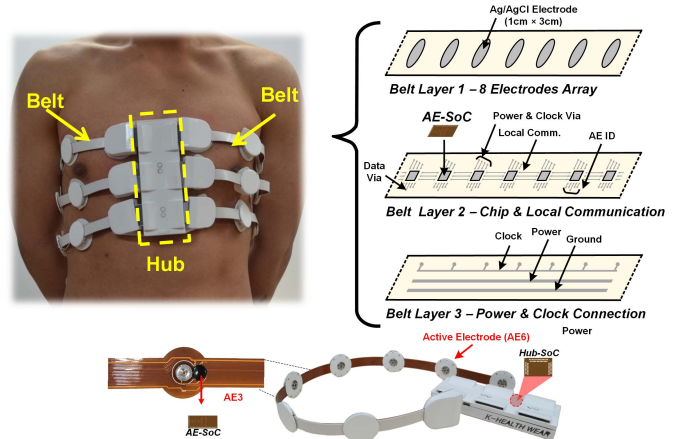


Fig. 4. Structure of the proposed System.

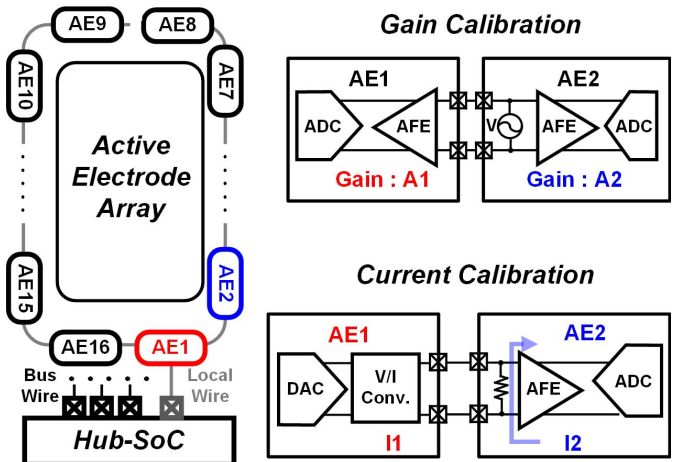


Fig. 5. System operation for gain and current compensation.

## II. SYSTEM REQUIREMENT AND OPERATION

### A. System Overview and Requirement

The overall system architecture of the proposed wearable 3-D lung ventilation monitoring system is shown in Fig. 1. It is composed of three functional components, which are electrode

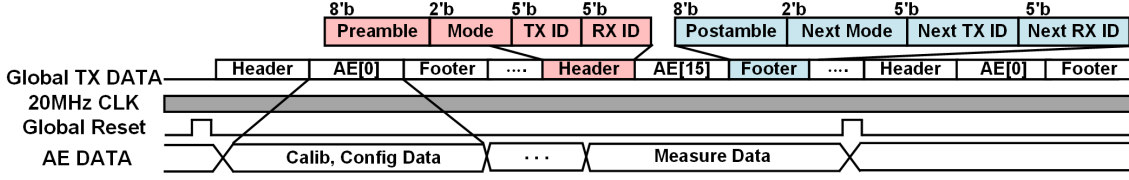


Fig. 6. Timing diagram of communication protocol for the proposed EIT system.

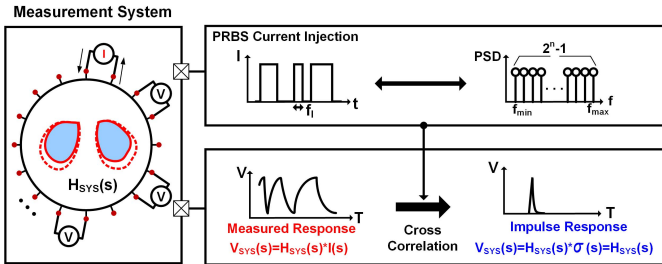


Fig. 7. MLS measurement in EIT system.

array, belt, hub of electronic circuitry, and an imaging device. The electrode array is made of wet-type electrodes, each of which is connected to a snap button of the belt. The belt contains a customized AE-SoC for signal sensing of 3-D resolution. The hub performs data gathering of three-plane belts and communication with the external imaging device using Bluetooth module. Finally, the lung EIT images are reconstructed and displayed on the external imaging device such as tablet computers or laptop. Fig. 2 shows the image reconstruction process and the detailed system requirement of the proposed system. Fig. 2(a) shows the brief algorithm of the proposed 3-D-EIT system. Thanks to Gauss-Newton iteration for the inverse solver, the conductivity of each element is updated, reducing the difference between measured and simulated voltages [13]. To achieve both high accuracy and low computational cost, the dual-model method which uses coarse model for the inverse solver and fine model for the forward solver is adopted. The number of elements for the fine model is more than 12,000, and EIDORS software is used to compute this EIT algorithm [14]. Fig. 2(b) shows the system requirement of the proposed 3-D-EIT system. To evaluate the performance, resolution error (RES) and position error (PE) are used [15]. Both of them are evaluated according to a number of electrode and belt plane. RES is evaluated by exchanging volume of the phantom in the center and outside of the cylinder, and PE is evaluated by moving the phantom from center to outside in the cylinder model. The mean error values of PE and RES are compared to ideal values. If the number of planes is less than 3, RES cannot be saturated. Similarly, PE is steadily  $< 0.10$  when the number of planes is  $\geq 3$ . To satisfy both figure-of-merits (FoMs) with the least number of electrodes, or the lowest hardware cost, it is necessary to take three-plane and 16-electrodes per plane. Although 3-D image reconstruction is possible by software, there is no 3-D-EIT system for lung ventilation monitoring because the impedance measurement for 3-D resolution is very difficult. Fig. 3(a) describes four major error sources in the 3-D-EIT measurement.

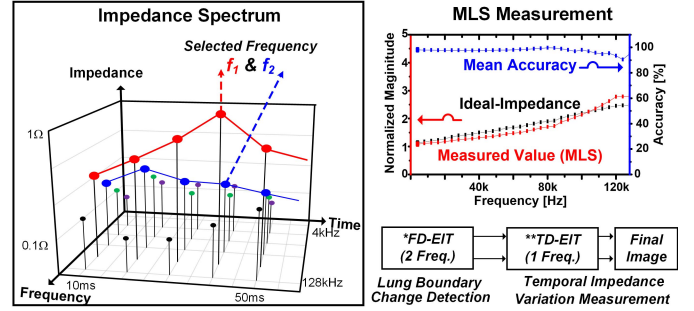


Fig. 8. Dual-mode current sensing procedure and measurement result.

First is the stray capacitance which becomes too large due to the long cable line wrapping the whole body. According to the measurement results of the stray capacitance in Fig. 3(b), up to 20% error is found in 60-cm cable. This stray capacitance error can be overcome by exploiting the AE system [16]. The second is the body modeling that was assumed by the previous EIT imaging methods for lung ventilation monitoring. Several imaging methods have been reported for EIT application, and among them, TD-EIT is widely used to get the lung image [11] because lung is a time varying organs. TD-EIT takes an initial measurement result as the reference data at time  $t_1$ , and posterior measurements result at time  $t_2$  ( $t_1 < t_2$ ) is compared with the reference data (the data at time  $t_1$ ) to get the impedance difference for the imaging. However, TD-EIT has limitations in extracting the lung boundary. To solve the problem, FD-EIT is adopted in [12], which is widely used for imaging static organs like breast cancer detection [22]. However, the two imaging methods still involve the problem of determining the optimal frequency of injection current because it should be varied depending on the individual patient due to personal lung impedance characteristics. Finding the frequency of injection current with the greatest conductivity difference at both TD-EIT and FD-EIT plays a significant role in improving the image resolution [12]. However, this value varies up to 60% depending on the individual [17]. Therefore, the optimal frequency of injection current for FD-EIT and TD-EIT corresponding to the measurement object should be found. Third problem is that the contact impedance of the current injection part and the voltage sensing part is changed. The variation between contact impedance of electrodes on the same subject may vary by up to 20% [18]. Therefore, high CMRR is required at the analog front-end (AFE) stage due to common-mode voltage, which is caused by high current amplitude at high frequency and contact impedance mismatch at the current injection electrode. Common-mode noise due to the contact impedance of current stimulator electrode is defined as (1) where  $H(s)$  is the transfer function of instruments

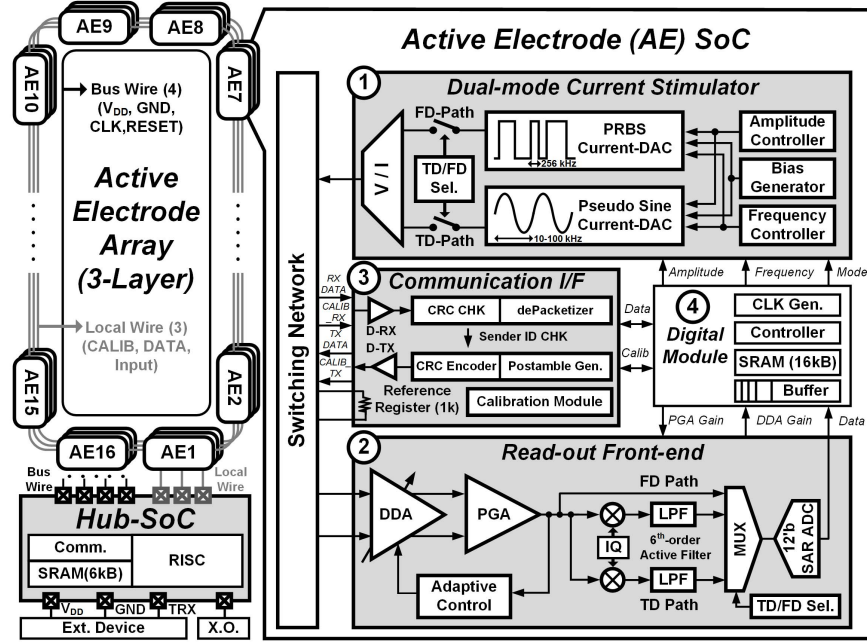


Fig. 9. Overall block diagram.

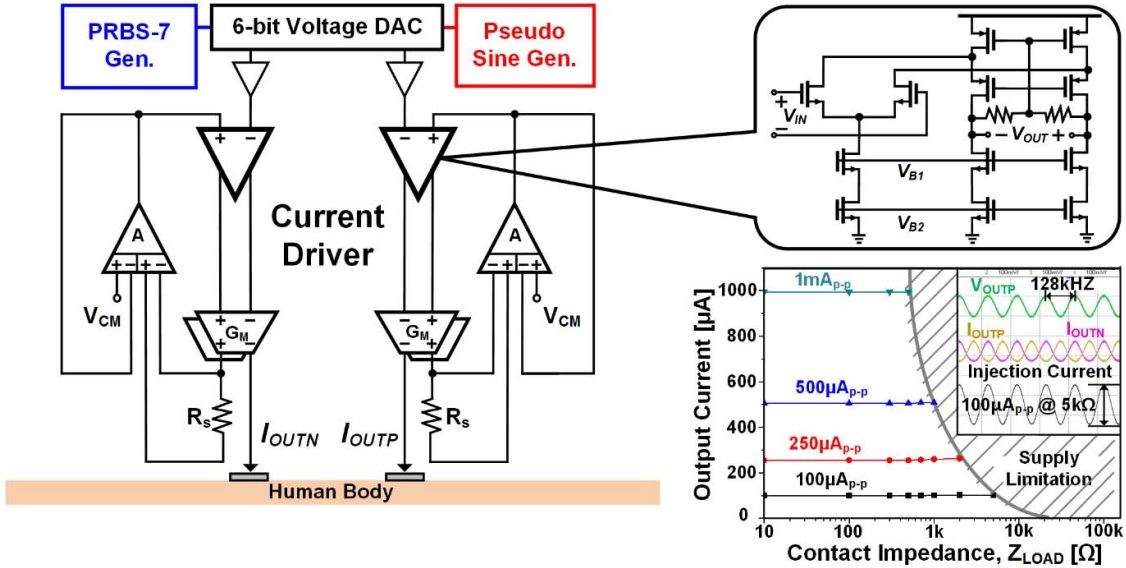


Fig. 10. Proposed dual-mode current stimulator.

amplifier (IA),  $I(s)$  is the injection current,  $Z_{LOAD}(s)$  is the load impedance, and  $CMRR(s)$  is the CMRR of IA

$$V_{OUT}$$

$$= H(s)I(s) \left[ Z_{LOAD}(s) \left\{ 1 + \frac{1}{2CMRR(s)} \right\} + \frac{Z_{CS}(s)}{CMRR(s)} \right]. \quad (1)$$

Also, the contact impedance mismatch of electrode causes a loading effect in IA and current stimulator. The effective load impedance is defined as (2) where  $Z_{CS}(s)$  is the contact impedance of current stimulator electrode,  $R_{O,CS}(s)$  is the output impedance of current stimulator,  $Z_{LOAD}(s)$  is the load impedance,  $Z_S(s)$  is the impedance of sensing electrode,

$\Delta Z_S(s)$  is the variation of the impedance of sensing electrode, and  $Z_{I,AMP}(s)$  is the input impedance of IA

$$Z_{LOAD,EFFECTIVE}(s) = \left\{ 1 - \frac{Z_{CS}(s)}{R_{O,CS}(s)} \right\} \times \left\{ Z_{LOAD}(s) + Z_{LOAD}(s) \frac{Z_S(s)}{Z_{I,AMP}(s)} + Z_S(s) \frac{\Delta Z_S(s)}{Z_{I,AMP}(s)} \right\}. \quad (2)$$

Since the maximal electrode contact impedance is  $500 \Omega$ , analyzing above equations leads to the requirements of high CMRR ( $>100$  dB), high input impedance ( $>1 \text{ m}\Omega$ ) of AFE, and high output impedance ( $>1 \text{ m}\Omega$ ) of the current stimulator in order to reduce error to  $<0.05\%$  at the worst contact impedance.

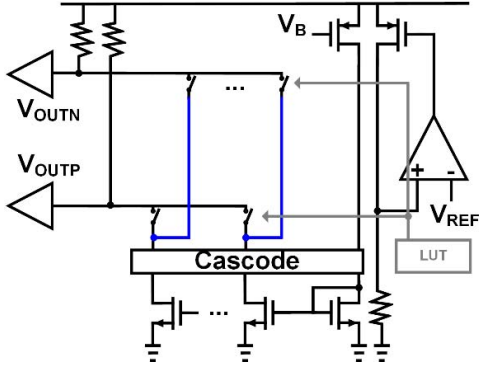


Fig. 11. Low-harmonic voltage DAC.

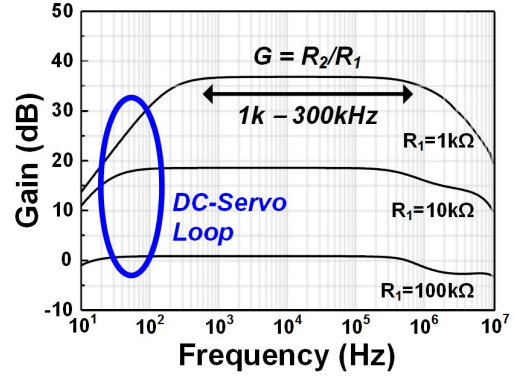


Fig. 14. Measured gain of the proposed IA.

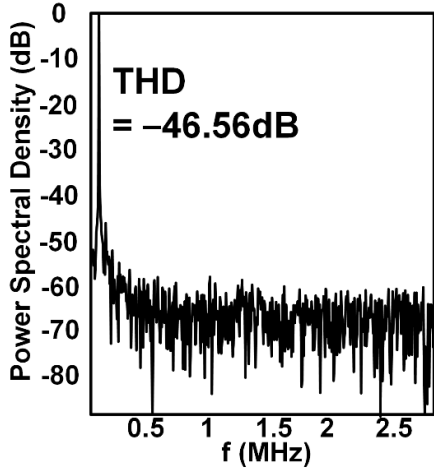


Fig. 12. Output spectrum of the proposed current stimulator.

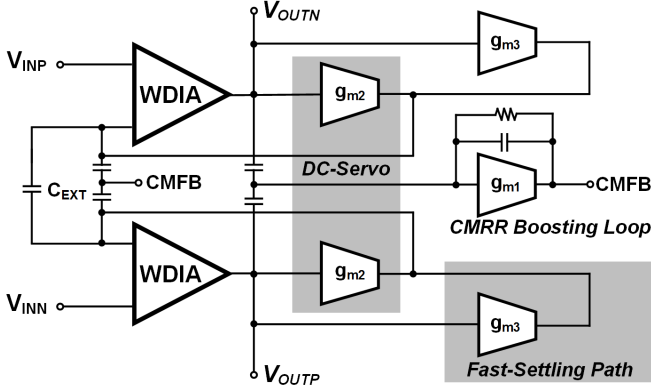


Fig. 13. Proposed wide dynamic range read-out front-end.

Fourth problem is that the measured voltage has a wide range of values. The measured voltage amplitudes at the adjacent pairs of electrodes are in the range of 0.01–40 mV according to the position of the electrode pair. The output voltage has a wide dynamic range because the maximum voltage is about 4,000 times of minimum voltage. Therefore, to detect such a small variation over a wide dynamic range ( $> 86 \text{ dB}$ )

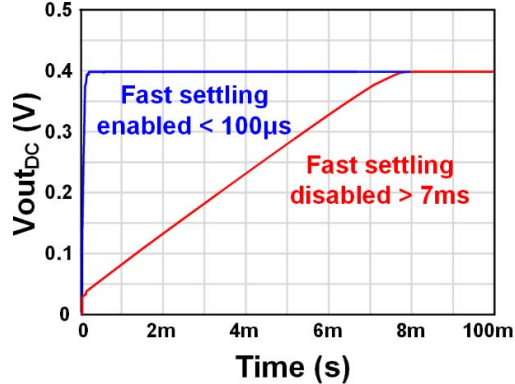


Fig. 15. Measured settling time with and without fast settling path.

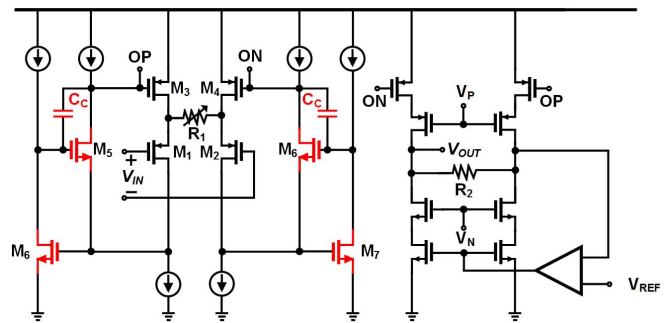


Fig. 16. Architecture of a core IA.

and high sensitivity ( $< 30 \text{ nV}/\sqrt{\text{Hz}}$ ) to sufficiently amplify minimum voltage signals.

### B. System Architecture and Operation

Fig. 4 shows the structures of the proposed system that allows simultaneous impedance sensing at 48 different channels. The three-plane system contains six belts in total, and a pair of belts forms a plane. Each belt is fabricated by flexible printed circuit board (FPCB) with eight AE-SoCs that shares single data bus line. And it supports 94 dB RX dynamic range and 32-tone frequency selection of TX. The Hub-SoC performs AE calibration, data collection, and wireless communication between an external device. Each FPCB belt (2-cm height) has three-layer: Layer-1 has eight wet-electrodes

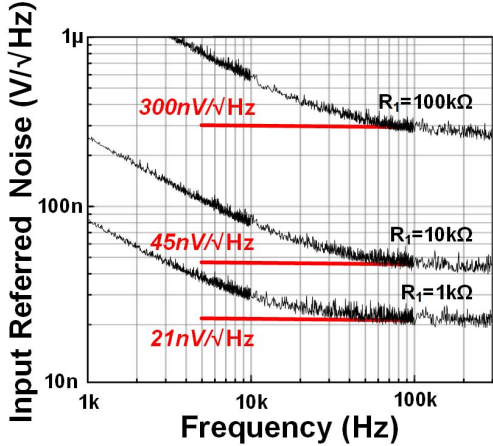


Fig. 17. Measured input-referred noise of front-end.

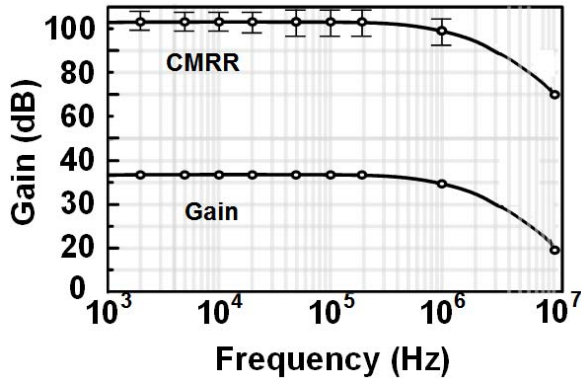


Fig. 18. Measured CMRR of IA.

of 2-in diameter. On Layer-2, eight AE-SoCs are bonded for the stable current injection and voltage measurement, and local communication lines connect each AE-SoC. Layer-3 provides power and clock signal to each AE-SoC of Layer-2. The connection to Hub-SoC is integrated on the edge of the belt. And measured electrode-skin contact impedance is less than  $500\ \Omega$ , which is sufficient to avoid signal saturation while  $1\ \text{mA}_{p-p}$  of differential current is used for EIT measurement under 1.2-V power supply.

The compensation process for the AE-SoC should be performed before starting the measurement because each AE-SoC has mismatch of channel gain and current amplitude. Fig. 5 shows the proposed current and gain compensation process. First, for the gain compensation of the AE, the reference current which is generated in AE[N] is applied to the reference resistance of AE[N+1]. And the voltage generated at that time is amplified at both AE[N] and AE[N+1], respectively. This process is sequentially performed from  $N = 1$  to 16, and the voltage ratio of the adjacent nodes is transmitted to the Hub-SoC. Next, for the current compensation, the current of AE[N] and AE[N+1] is applied to the reference resistors of AE[N+1], respectively, and the ratio of amplified voltage is also transmitted to the hub. This process is repeated likewise for all the AE nodes. The detail calibration transactions between AE-node and Hub are also

TABLE I  
BIO-IMPEDANCE READ-OUT FRONT-END COMPARISON

|  | L. Yan<br>JSSC 2011                 | W. Lee<br>JSSC 2015 | L. Yan<br>T-BioCAS 2013              | This Work                           |
|--|-------------------------------------|---------------------|--------------------------------------|-------------------------------------|
| Technology                               | 0.18 $\mu\text{m}$                  | 0.11 $\mu\text{m}$  | 0.18 $\mu\text{m}$                   | 65 nm                               |
| Supply                                   | 1.2 V                               | 1.2 V               | 1.8 V                                | 1.2 V                               |
| Gain                                     | 66-88 dB<br>(4 step)                | 50-80 dB            | 30.5-56.5 dB<br>(6 step)             | 20-70 dB<br>(5 step)                |
| Diff. input range                        | 0.23 mV <sub>p-p</sub>              | N/A                 | 0.18 $\mu\text{m}$                   | 50 mV <sub>p-p</sub>                |
| Input noise floor                        | 58 nV/sqrt(Hz)                      | N/A                 | 149 nV/sqrt(Hz)                      | 21 nV/sqrt(Hz)                      |
| Input RMS noise<br>(1 range)             | 409 nV <sub>rms</sub><br>(0.5-50Hz) | N/A                 | 1053 nV <sub>rms</sub><br>(0.5-50Hz) | 148 nV <sub>rms</sub><br>(0.5-50Hz) |
| Dynamic Range                            | 39 dB                               | N/A                 | 83 dB                                | 94 dB                               |
| Input Impedance                          | 1 M $\Omega$                        | 800 k $\Omega$      | 20 M $\Omega$                        | 18 M $\Omega$                       |
| CMRR                                     | 91 dB                               | 76 dB               | 114 dB                               | 100 dB                              |
| Offset Rejection                         | N/A                                 | N/A                 | N/A                                  | 400 mV                              |
| Max Frequency<br>of Injection<br>Current | 90 kHz                              | 64 kHz              | 20 kHz                               | 256 kHz                             |
| Current                                  | 33 $\mu\text{A}$                    | 60 $\mu\text{A}$    | 1.2 $\mu\text{A}$                    | 41 $\mu\text{A}$                    |
| FoM                                      | 179                                 | -                   | 113                                  | 28.4                                |

$$\text{FoM} = \text{Vrms,noise(nV)} * \text{Power}(\mu\text{W}) / \text{Current Bandwidth (kHz)}$$

shown in Fig. 6. Each node sends the calibration data to the Hub-SoC through the shared global wire. The data is packetized to have a header (20-bit), a variable size data (30–220-bit) depending on operating modes, and a footer (20-bit). Gain and current compensations are performed only once in the beginning. The measurement starts after both gain and current are compensated, which reduces the variation to less than 0.8 mV among 48 AEs.

At the beginning of the measurement, dual-mode current sensing using the maximum length sequence (MLS) method is applied to the system, which is widely used to obtain the transfer function of the system [19]. Fig. 7 shows the detailed procedure of the proposed impedance spectrum sensing in EIT system. Unlike conventional current injection for impedance acquisition, MLS injects the pseudorandom binary sequence (PRBS) current, which has even power spectrum with small interval frequency. The measured voltage response shows the product of the system response and the injection current. Cross correlation of input and output shows the impulse response of the system, and the transfer function of the system can be obtained. MLS can be applied in EIT since it is approximately a linear time invariant system. Fig. 8 shows the frequency selection process and measurement result of the proposed impedance spectroscopy. MLS currents are generated by 256-kHz PRBS-7 for wide-band frequency measurement from 4 to 128 kHz with 4-kHz intervals, simultaneously. Two frequencies that show the biggest temporal impedance difference are chosen from averaged impedance spectrum for FD-EIT which will be used to delineate the boundary of a human lung. After FD-EIT, TD-EIT with one-tone frequency is performed for lung volume change detection. Compared to conventional lung monitoring EIT IC [12] which provides FD-EIT and TD-EIT at the same time and measured with two fixed frequencies, the proposed technique provides wide FD-EIT and TD-EIT stimulation current

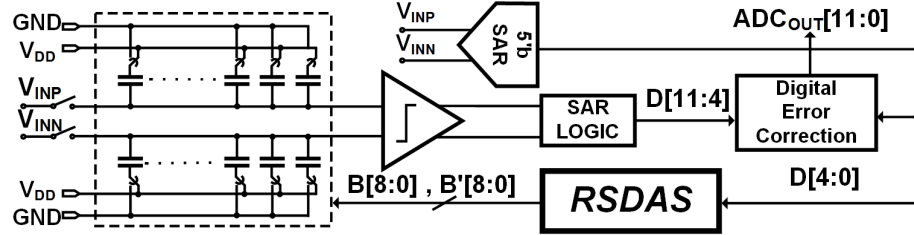


Fig. 19. Proposed auto calibration SAR ADC architecture.

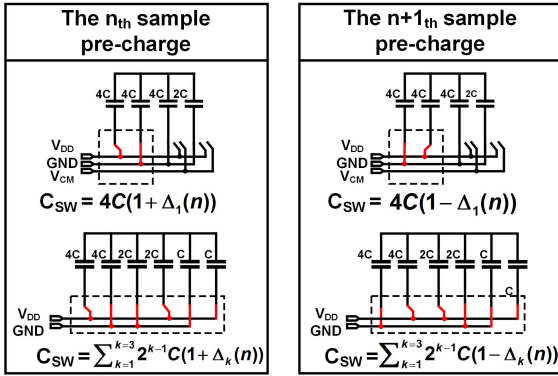


Fig. 20. RSDAS.

frequency according to the patient to improve accuracy. The measured impedance variation from MLS across 48 electrodes shows 92% mean accuracy compared with the ideal impedance value which is measured with one-tone frequency as depicted in Fig. 8.

### III. ELECTRICAL IMPEDANCE TOMOGRAPHY SOC

Fig. 9 shows the overall block diagram of the Hub-SoC and AE-SoC, and network topology connecting 48 AE-SoCs to 1 Hub-SoC. The AE-SoC is composed of a dual-mode current stimulator, an impedance read-out front end for wide-band data acquisition, a communication I/F to interconnect with other 15 AE nodes and the Hub, a digital module with 16-kB on-chip SRAM for switching control, pre-processing, data storing, and data transferring to Hub-SoC. The Hub chip is composed of a communication I/F with 6-kB SRAM for data collection from AE nodes and an reduced instruction set computer (RISC) for communication to the external device.

#### A. Dual-Mode Current Stimulator

The current stimulator is one of the most important part in the EIT measurement. Several current stimulator designs have been reported for the EIT system. First, Halter *et al.* [20] and Lee *et al.* [21] utilized FPGA-based direct digital synthesizer to implement current stimulators, but they were bulky and showed low accuracy. Second, Hong *et al.* [11], [22] implemented the current stimulators by using a Wien-bridge oscillator with low total harmonic distortion (THD), but they suffered from large power consumption and small output impedance. Also, they cannot be used for active electrode (AE) systems because

they are analog-based control, which cannot control stimulation frequency of all the AE nodes constantly. Third, Lee *et al.* [12] utilized pseudo-sine current stimulator which is widely used for bio-impedance measurements [23]. But there are several limitations when injection frequency is more than several tens of kilohertz due to its digital-to-analog converter (DAC) architecture. First, its low output impedance introduces current attenuation. Second, PMOS and NMOS mismatch and glitch at switching node introduces frequency harmonic that degrades injection current accuracy. To overcome the previous shortcomings, a dual-mode current stimulator circuit is proposed as shown in Fig. 10, which is composed of a low-harmonic 6-bit voltage DAC, a PRBS-7 lookup table (LUT), a pseudo-sine LUT, and a high output impedance current driver. A sense resistor  $R_s$  is used to monitor the output current, and it enables the current driver to have a negative feedback. It allows the output impedance to be large as (3) where  $r_o$  and  $G_m$  are the small-signal output resistance and the gain of the transconductor  $G_M$  and  $A$  is the gain of differential-to-differential amplifier.

$$Z_{\text{OUT}} \approx A \times G_M \times r_o \times R_s. \quad (3)$$

The measured output impedance of the current driver shows 1.3 mΩ at 256 kHz. A folded cascode amplifier is used for loop stability and the current driver injects four stable currents (0.1, 0.25, 0.5, and 1 mA) in the frequency range of 10–256 kHz over a wide variation of contact impedance from 10 Ω to 100 kΩ, as shown in Fig. 10. Measured current values show <0.1% error up to 100-kΩ load variation. Also, the previous pseudo-sine structure uses both NMOS and PMOS which causes harmonic distortion due to its mismatch, and a glitch occurs at the switching node resulting in harmonic distortion when the switching frequency goes up. Fig. 11 shows the proposed low harmonic voltage DAC architecture. Only NMOS is used to reduce the mismatch between PMOS and NMOS, and differential sampling was performed to reduce glitch in the switching node. The instantaneous current does not flow when the switching occurs, because the current continuously flows into all the branches so that the harmonic is greatly reduced and the result is shown in Fig. 12. The measured THD is less than 0.5% at 128 kHz.

#### B. Wide Dynamic Range Readout Front End

Fig. 13 shows the proposed wide dynamic range sensor circuit. Differential-to-differential architecture (DDA) is adopted to increase input impedance and CMRR. Because the inherent

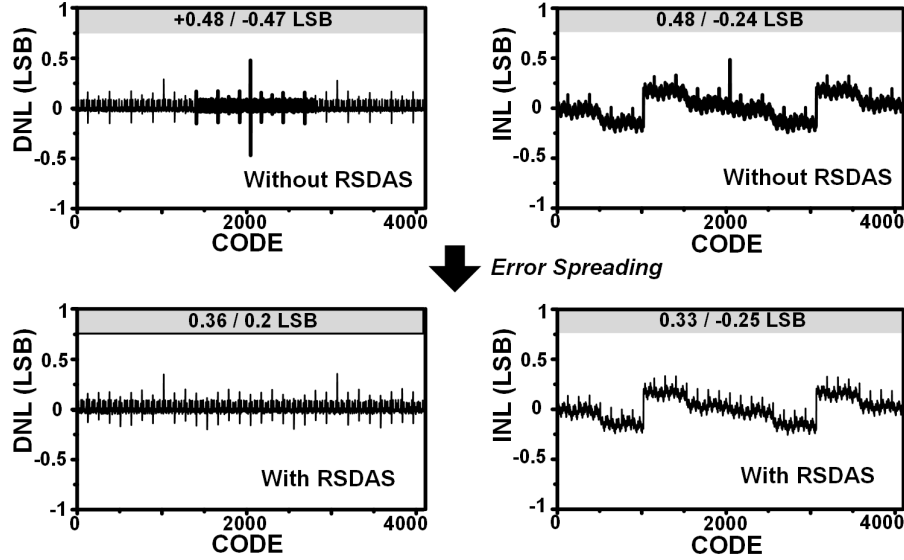


Fig. 21. Measured INL, DNL of the proposed SAR ADC.

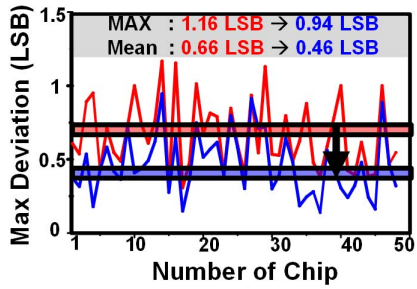


Fig. 22. Measured deviation versus number of chip.

structure characteristics of the DDA is the direct connection between the human body and input MOS, the input impedance is  $>18\text{ m}\Omega$  at 100 kHz. The proposed DDA uses three loops for sensing bio-impedance signal. For high CMRR, CMRR boosting loop of  $g_{m1}$  is added to reject common-mode signal. It extracts the common-mode signals of the output by averaging, and then feeds it back to the inputs with negative feedback. This cancels out the common-mode input before signals are amplified. Second, dc servo loop (DSL) is added to remove dc offset up to 400 mV. The DSL consists of a  $G_m$ -C integrator that monitors the output offset and cancels it by driving the input of wide dynamic range IA (WDIA).  $G_m$ -C integrator utilizes a weak transconductance of  $g_{m2} = 1\mu\text{S}$  and an external capacitor (10 nF) for a low cutoff frequency (100 Hz). The gain is controlled by the peak detector [20], and the resulting gain is shown in Fig. 14. The measured three-level gains and noise floors are 37.52, 18.43, and 0.74 dB, and the low frequency cutoff is determined by the DSL. Third, fast settling loop is added to reduce settling time when electrode switching occurs in the EIT system operation. In the EIT measurement process, the stimulation electrode and the voltage measuring electrode should be changed 48 times to obtain one frame of image. If the settling time becomes longer than impedance measurement

time of an electrode, the frame rate decreases. To prevent the problem, sensor settling time should be short enough to ensure that it settles before the electrode switching for fast EIT operation and  $g_{m3}$  ( $= g_{m2} \times 100$ ) enables to reduce settling time up to 100  $\mu\text{s}$  as shown in Fig. 15. Fig. 16 shows the detailed transistor-level schematic of the proposed single WDIA. The design is based on previous current feedback IA architecture for bio-impedance sensing [24], but expanded to support a wide dynamic input range, which is required to ensure a wide EIT input signal range as mentioned in the previous chapter. Also, the readout front end is the most power-consuming part because it operates in 48-AE simultaneously, while one current stimulator operates only out of 48-AE at a time. Therefore, low-power design is also required.

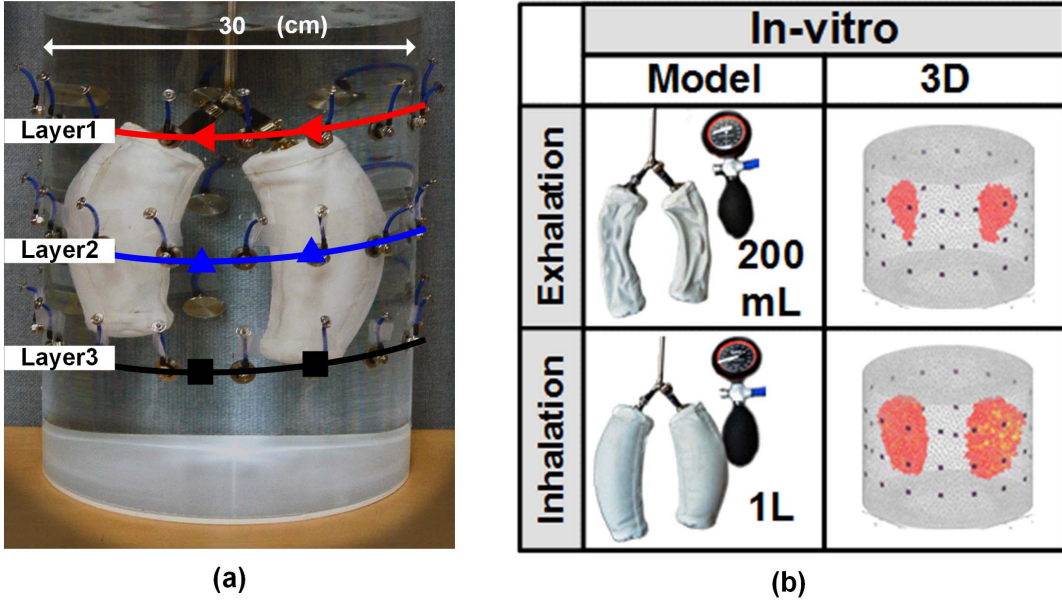
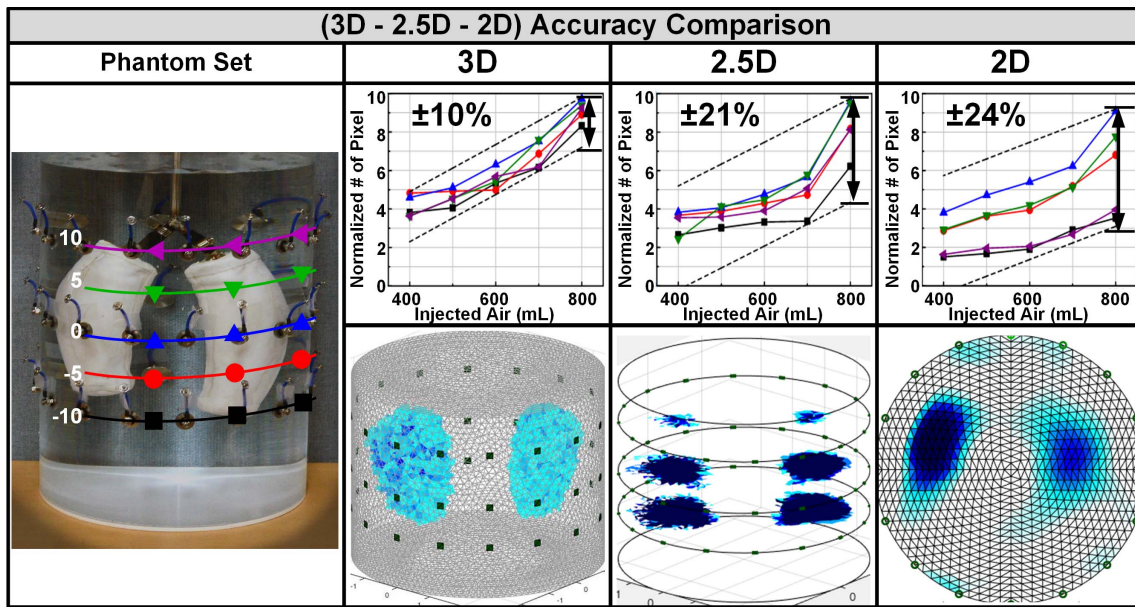
The input dynamic range is limited by the requirement that the input-referred noise should be low where the exact value is determined by input signal amplitude. In [24] and the proposed architecture, input-referred noise is determined as follows:

$$V_{ni,IA}^2 \approx 2V_{M1}^2 + V_{R1}^2. \quad (4)$$

Under the same current consumption, resistor  $R_1$  is the main source of input-referred noise. Therefore, small  $R_1$  is needed to achieve lower noise. However, large bias current is required in [24] when the input signal is large. Also, Yazicioglu *et al.* [24] adopt flipped voltage follower Carvaljal *et al.* [25] and the corresponding source node impedance of input pair is (5), which is insufficient for small input voltage signal

$$Z = \frac{1}{g_{m1}g_{m3}r_{o1}}. \quad (5)$$

To solve the above problem, the gain of WDIA is controlled in three different levels by tuning the value of  $R_1$  according to the output voltage of the final programmable gain amplifier using

Fig. 23. (a) *In vitro* measurement setup. (b) Imaging result of *in vitro* measurement.Fig. 24. Comparison of *in vitro* measurement versus measurement dimension.

the peak detector. To improve the linearity of the conventional flipped voltage follower, the gain-boosting is adopted using  $M_6$  and  $M_7$  transistors. It stabilizes  $M_{1,2}$  drain voltages to keep their operation stable. This also allows  $M_{1,2}$  to maintain their source follower functionality even when WDIA drives the low values of  $R_1$  because source node impedance of input pair is effectively reduced by a factor of  $(g_m r_o)^2$  as follows:

$$Z = \frac{1}{g_m g_m r_o (g_m r_o)^2}. \quad (6)$$

Also, the MILLER compensation capacitor  $C_c$  between  $M_{5,6}$  gate and drain is added to enhance loop stability. As a result, WDIA supports more than 50-mV<sub>p-p</sub> input voltage range with THD less than 1%. Fig. 17 shows the measured three-level

noise floors of 21, 45, 300 nV/Hz, and the corresponding noise levels are determined by the input amplitude [1V, 0.1 mV], [0.1 mV, 10 mV], and [10 mV, 100 mV], respectively.

Fig. 18 shows the results of the CMRR measurement. The bars in the plot represents the maximum spread from 100 chips. Within a measurement frequency of 300 kHz, the 100 chip measurements yielded the maximum of 108 dB and the minimum of 93 dB, respectively. Table I shows the comparisons with the recent bio-impedance read-out front-end circuits that includes IA and its bias power. A new FoM is used for comparison to consider power consumption, noise level, and bandwidth. It takes the bandwidth into account because WDIA has much wider bandwidth than the existing bio-impedance readout. The proposed front end represents

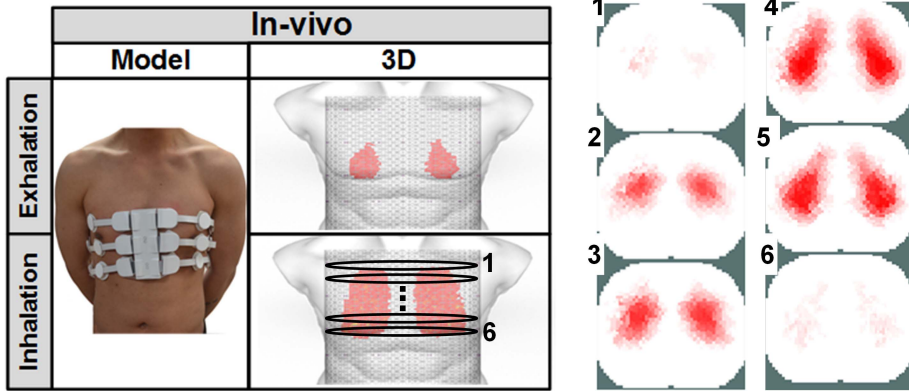
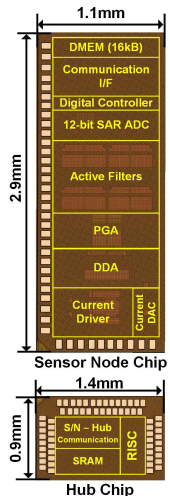
Fig. 25. *In vivo* measurement setup and imaging result.

Fig. 26. Chip microphotograph.

the lowest noise (21 nV/Hz) and the highest dynamic range (94 dB).

### C. Auto Calibration SAR ADC

Fig. 19 shows the block diagram of the proposed SAR ADC. It consists of a 5-bit coarse-SAR ADC, a 10-bit fine-SAR ADC, and a digital error correction block to reduce the DAC mismatch using one redundancy bit. In addition, we proposed the random swapping scheme for linearity using split cap architecture. At the same time, detecting and skip switching [26] is adopted to reduce the switching power consumption in the split cap architecture and the 82% switching power reduction was achieved. Fig. 20 shows the detailed random swapping process. When the ADC samples the voltage, its switching capacitance value is  $4C(1 + \Delta)$  which generates voltage error due to  $4C\Delta$ . If the value of the pre-charging capacitor of the  $(n + 1)$ th sampling step is different from the  $n$ th capacitor, the voltage error becomes  $4C(1 - \Delta)$  and the resulting error can be averaged out to 0.

If we expand the proposed switching to more MSB-side capacitors, we can get more averaging effect in the split cap DAC architecture. In this case, the capacitors from MSB to MSB-3 are swapped randomly during pre-charging to enhance

TABLE II  
CHIP PERFORMANCE SUMMARY

| Process   |   | 65 nm Mixed CMOS   |                                    |
|---|---|--|------------------------------------|
| Die Size  |   | Sensor-Node Chip : 1.1 x 2.9 mm<br>Hub Chip : 1.4 x 0.9 mm |                                    |
| Supply Voltage  |   | 1.2 V  |                                    |
| Power Consumption   |   | 6.96 mW  |                                    |
| S<br>E<br>N<br>S<br>O<br>R<br>N<br>O<br>D<br>E                | Dual-mode Current Stimulator            | Frequency  | 10 ~ 256 kHz (20 step)             |
|   |   | Amplitude  | 0.1 ~ 1 mA <sub>p-p</sub> (4 step) |
|   |   | Output Impedance   | 1.3 MΩ @ 256 kHz                   |
|   |   | THD  | < 0.5 %                            |
| R<br>E<br>A<br>D<br>O<br>U<br>T<br>F<br>R<br>E<br>E<br>N<br>D | Read-Out Front-End                      | Gain   | 20 ~ 70 dB (6 step)                |
|   |   | Bandwidth  | 300 kHz                            |
|   |   | Input Noise  | 21 nV / √Hz                        |
|   |   | CMRR   | > 100dB @ 100kHz                   |
|   |   | Offset-Rejection   | 400 mV                             |
|   |   | Input Impedance  | 18 MΩ                              |
| C<br>O<br>M<br>M<br>U<br>L<br>T<br>I<br>C<br>S                | Communication I/F w/ Digital Controller | Operating Freq   | 20 MHz                             |
|   |   | On-chip SRAM   | 16 kB                              |
|   |   | Power Consumption  | 1.1 mW                             |
| H<br>U<br>B   | Communication I/F w/ RISC               | On-chip SRAM   | 6 kB                               |

TABLE III  
PERFORMANCE SUMMARY COMPARED WITH STATE-OF-THE-ART EIT ICs

|                        | ISSCC'14 <sup>[21]</sup> | ASSCC'14 <sup>[11]</sup>       | SoVC'15 <sup>[12]</sup>        | This Work                      |
|------------------------|--------------------------|--------------------------------|--------------------------------|--------------------------------|
| Application            | Breast Cancer Detecting  | 2D-Lung Ventilation Monitoring | 2D-Lung Ventilation Monitoring | 3D-Lung Ventilation Monitoring |
| # of Electrodes        | 90                       | 32                             | 32                             | 48                             |
| Power Consumption      | 53.4 mW (except imaging) | 10.4 mW (except imaging)       | 4.84 mW (except imaging)       | 6.96 mW (except imaging)       |
| Power / Electrodes     | 0.59 mW                  | 0.33 mW                        | 0.15 mW                        | <b>0.145 mW</b>                |
| # of Frequencies (FD)  | 4                        | 1                              | 2                              | <b>16</b>                      |
| Freq. Selectivity (TD) | X                        | Fixed                          | Fixed                          | User Selective                 |
| Frame Rate of AFE      | 1 fps                    | ~ 20 fps                       | ~ 30 fps                       | <b>~ 70 fps</b>                |
| Active Electrode       | X                        | X                              | X                              | O                              |
| Dynamic Range          | 80 dB                    | 79 dB                          | N/A                            | <b>94 dB</b>                   |

the swapping effect with further suppression of DAC error. Fig. 21 shows the measured DNL and INL plots before and after applying the proposed random swapping detect and skip (RSDAS) scheme. Before applying RSDAS, the peak DNL and INL are 0.48–0.47 and 0.48–0.24 LSB, respectively.

TABLE IV  
SYSTEM COMPARISON TABLE

|                                      | <b>Sheffield</b>  | <b>Dragger</b>  | <b>S. Hong<br/>ASSCC-2014</b>   | <b>This Work</b>  |
|--------------------------------------|---|---|---|---|
|                                      |  |  |  |  |
| <b>Application</b>                   | Lung Ventilation Monitoring   | Lung Ventilation Monitoring   | Lung Ventilation Monitoring   | Lung Ventilation Monitoring   |
| <b>Size</b>                          | 1550 x 570 x 640 mm   | 600 x 1400 x 750 mm   | 860 x 40 x 2 mm   | 1120 x 240 x 5 mm   |
| <b>Electrodes</b>                    | 8 electrodes + 1 ref.   | 16 electrodes + 1 ref.  | 32 electrodes   | 16 electrodes x 3 layers (48 electrodes)  |
| <b>Reconstructed Image Dimension</b> | <b>2D</b>   | <b>2D</b>   | <b>2D</b>   | <b>3D</b>   |
| <b>Power Consumption</b>             | N/A   | 80 W  | 10.4 mW   | <b>6.96 mW</b>  |
| <b>Frequency</b>                     | 2 kHz ~ 1.6 MHz   | 80 ~ 130 kHz  | 10 ~ 200 kHz  | <b>10 ~ 256 kHz</b>   |
| <b>Current Amplitude</b>             | 276 $\mu$ A <sub>p-p</sub>  | N/A   | 0.1 ~ 1 mA <sub>p-p</sub>   | 0.1 ~ 1 mA <sub>p-p</sub>   |
| <b>Frame Rate</b>                    | 25 fps  | 10, 15, 20, or 30 fps   | Up to 20 fps  | <b>Up to 10 fps</b>   |

There is a severe glitch in the middle code due to capacitor mismatch. After applying RSDAS, the peak DNL and INL are reduced to 0.36–0.2 and 0.33–0.25 LSB. The error at the middle code spreads to the location of one-quarter and three-quarter code due to the averaging effect. Fig. 22 shows the measured INL/DNL of 48 AE-SoCs. The measured maximum deviation across 48 AE chips decreases from 0.66 to 0.46 LSB. The sampling rate of the ADC depends on the system operation modes. The ADC operates at 256 kHz in MLS-mode, however, its energy consumption is negligible because the MLS-mode operates very shortly in the measurement which takes only 2% in the total operation time. In TD-EIT and FD-EIT modes, the sampling rate is reduced up to 10 kHz depending on the injection current frequency because the input signal is demodulated. Therefore, the ADC consumes only  $\sim$ 1 W of power in both TD-EIT and FD-EIT modes, which is ignorable in the overall system power.

#### IV. IMPLEMENTATION RESULT

##### A. System Measurement Results

The proposed wearable 3-D lung ventilation monitoring system with EIT-SoC was first verified by *in vitro* measurements. Fig. 23(a) shows the measurement setup. The body model test phantom is made of a water tank of 30-cm diameter and two lung-shaped balloons. The lung-shaped balloons can be inflated up to 1 L of volume. The belt-type system is put around by a snap button to the test phantom. The system is connected to the PC via Bluetooth communication to reconstruct 3-D-EIT image as well as to gather measured raw impedance data. The reconstructed 3-D images are visualized as 150,000 meshes in a cylinder model for *in vitro* test and the torso model for *in vivo* test. Fig. 23(b) shows the imaging result of the test phantom of 200 mL and

1 L volume, respectively. To verify the performance of the proposed EIT system, the phantom image is reconstructed by three ways: 1) 2-D reconstruction using impedance data of 1-plane ( $16 \times 14$  data); 2) 2.5-D reconstruction using three-planes impedance data without information exchange between other planes ( $3 \times 16 \times 14$  data); and 3) 3-D reconstruction using three-planes impedance data with information exchange between other planes ( $3 \times 3 \times 16 \times 14$  data).

Fig. 24 shows the resulted images and measured plots of the test phantom according to the measurement dimension. For quantitative analysis, the number of pixels, in which the conductivity is changed over threshold over the whole 150,000 pixels of reconstructed image, are counted and plotted with respect to the injected air volume. The graph shows the change in volume as the center of the phantom is moved vertically from  $-10$  to  $10$  cm in the water tank. The 3-D-images show much accurate volume information, which is  $\pm 10\%$ , compared with 2-D-EIT ( $\pm 24\%$ ) and 2.5-D-EIT ( $\pm 21\%$ ) images. The reconstructed 3-D-EIT images can detect volume change over 90% accuracy even though electrode positions are changed relative to the lung position ( $-10$  to  $10$  cm) while 2-D-EIT shows severe accuracy degradation. Fig. 25 shows the *in vivo* measurement results with the human body. The spontaneous breathing of human subjects is measured with 0.5 mA of current at 100 kHz. The two lungs are clearly displayed with real-time operation. The upper image in the left figure is reconstructed using reference data measured at exhalation, and the bottom image is reconstructed using reference data at inhalation. The single-plane images in right figure represent 2-D reconstructed images according to the belt position from 1 to 6. As can be seen clearly from the measurement results, the lung images greatly vary depending on the belt position, and the 3-D-EIT shows much stable image in lung ventilation monitoring.

### B. IC Implementation Result

Fig. 26 shows the chip micrograph and the system performance summary. The AE-/Hub-SoCs are fabricated in 65-nm 1P6M Mixed CMOS and occupy 3.2 and 1.3 mm<sup>2</sup>, respectively. The performance of the proposed EIT-SoC is summarized in Table II. Average power consumption is 124  $\mu$ W for the AE chip and 1.1 mW for the Hub-SoC. The proposed dual-mode current stimulator can provide 20 steps of stimulation frequency and four amplitude steps. It shows the 1.3-m $\Omega$  output impedance and achieves less than 0.5% THD. The read-out front end adaptively controls its gain from 20 to 70 dB (six-step) with the input-referred noise of 21 nV/ $\sqrt{\text{Hz}}$ . The digital controller containing 16-kB on-chip SRAM operates at 20 MHz. The IC comparison results with previous EIT chips are shown in Table III. The proposed EIT-SoC shows the lowest power-per-electrode of 0.145 mW with the highest RX dynamic range of 94 dB. Also, the proposed SoC provides user selective stimulation frequency of FD-EIT and TD-EIT. The system comparison results with previous lung ventilation monitoring are shown in Table IV. The proposed lung ventilation monitoring system shows the lowest power consumption of 6.96 mW with very small form factor and lightweight. Moreover, it can provide 3-D lung images in real-time up to 10 frames/s.

### V. CONCLUSION

In this paper, the EIT-SoC for the high-quality impedance acquisition is designed for the wearable 3-D real-time lung ventilation monitoring system. The dual-mode current stimulator provides the optimal frequency for TD-EIT and FD-EIT with simultaneous 4–128 kHz impedance sensing. In addition, the WDIA provides 94-dB dynamic range impedance sensing. Moreover, the 48-channel active electrodes system with dedicated communication and calibration is implemented to reduce coupling noise. As a result, 1.4-m $\Omega$  sensitivity of impedance difference is achieved in the *in vivo* environment. Thanks to the proposed SoCs, the overall system can detect volume change over 90% accuracy even though electrode positions are changed relative to the lung position (−10 to 10 cm) while 2-D-EIT shows large amount of accuracy degradation. As a result, the first wearable real-time 3-D lung ventilation monitoring system is successfully implemented.

### REFERENCES

- [1] L. N. Tremblay and A. S. Slutsky, “Ventilator-induced lung injury: From the bench to the bedside,” *Applied Physiology in Intensive Care Medicine*, M. R. Pinsky, L. Brochard, G. Hedenstierna, and M. Antonelli, Eds. New York, NY, USA: Springer, 2012, pp. 343–352.
- [2] G. D. Rubenfeld *et al.*, “Incidence and outcomes of acute lung injury,” *N. England J. Med.*, vol. 353, no. 16, pp. 1685–1693, Oct. 2005.
- [3] R. L. Doyle, N. Szaflarski, G. W. Modin, J. P. Wiener-Kronish, and M. A. Matthay, “Identification of patients with acute lung injury. Predictors of mortality,” *Amer. J. Respirat. Critical Care Med.*, vol. 152, no. 6, pp. 1818–1824, 1995.
- [4] M. D. Zilberberg and S. K. Epstein, “Acute lung injury in the medical ICU: Comorbid conditions, age, etiology, and hospital outcome,” *Amer. J. Respirat. Critical Care Med.*, vol. 157, no. 4, pp. 1159–1164, 1998.
- [5] P. Blankman and D. Gommers, “Lung monitoring at the bedside in mechanically ventilated patients,” *Current Opinion Critical Care*, vol. 18, no. 3, pp. 261–266, 2012.
- [6] R. Ochiai, “Mechanical ventilation of acute respiratory distress syndrome,” *J. Intensive Care*, vol. 3, no. 1, p. 25, 2015.
- [7] D. S. Holder, *Electrical Impedance Tomography: Methods, History and Applications*. Bristol, U.K.: IOP Publishing, 2005.
- [8] A. J. Wilson, P. Milnes, A. R. Waterworth, R. H. Smallwood, and B. H. Brown, “Mk3.5: A modular, multi-frequency successor to the Mk3a EIS/EIT system,” *Physiol. Meas.*, vol. 22, no. 1, pp. 49–54, Feb. 2001.
- [9] C. Gómez-Laberge, J. H. Arnold, and G. K. Wolf, “A unified approach for EIT imaging of regional overdistension and atelectasis in acute lung injury,” *IEEE Trans. Med. Imag.*, vol. 31, no. 3, pp. 834–842, Mar. 2012.
- [10] G. K. Wolf *et al.*, “Mechanical ventilation guided by electrical impedance tomography in experimental acute lung injury,” *Critical Care Med.*, vol. 41, no. 5, pp. 1296–1304, May 2013.
- [11] S. Hong, J. Lee, J. Bae, and H.-J. Yoo, “A 10.4 mW electrical impedance tomography SoC for portable real-time lung ventilation monitoring system,” in *Proc. IEEE A-SSCC*, Nov. 2014, pp. 193–196.
- [12] Y. Lee, K. Song, and H.-J. Yoo, “A 4.84 mW 30 fps dual frequency division multiplexing electrical impedance tomography SoC for lung ventilation monitoring system,” in *Proc. IEEE Symp. VLSI Circuits*, Jun. 2015, pp. C204–C205.
- [13] B. Grychtol, B. Müller, and A. Adler, “3D EIT image reconstruction with GREIT,” *Physiol. Meas.*, vol. 37, no. 6, pp. 785–800, May 2016.
- [14] M. Vauhkonen, W. R. B. Lionheart, L. M. Heikkinen, P. J. Vauhkonen, and J. P. Kaipio, “A MATLAB package for the EIDORS project to reconstruct two-dimensional EIT images,” *Physiol. Meas.*, vol. 22, no. 5, pp. 11–107, 2001.
- [15] A. Adler *et al.*, “GREIT: A unified approach to 2D linear EIT reconstruction of lung images,” *Physiol. Meas.*, vol. 30, no. 6, pp. S35–S55, Jun. 2009.
- [16] P. O. Gaggero, A. Adler, J. Brunner, and P. Seitz, “Electrical impedance tomography system based on active electrodes,” *Physiol. Meas.*, vol. 33, no. 5, pp. 831–847, 2012.
- [17] C. Gabriel, A. Peyman, and E. H. Grant, “Electrical conductivity of tissue at frequencies below 1 MHz,” *Phys. Med. Biol.*, vol. 54, no. 16, pp. 4863–4878, 2009.
- [18] A. McEwan, A. Romsauerova, R. Yerworth, L. Horesh, R. Bayford, and D. Holder, “Design and calibration of a compact multi-frequency EIT system for acute stroke imaging,” *Physiol. Meas.*, vol. 27, no. 5, pp. 199–210, 2006.
- [19] T. Sun, D. Holmes, S. Gawad, N. G. Green, and H. Morgan, “High speed multi-frequency impedance analysis of single particles in a microfluidic cytometer using maximum length sequences,” *Lab Chip*, no. 7, no. 8, pp. 1034–1040, Aug. 2007.
- [20] R. Halter A. Hartov, and K. D. Paulsen, “Design and implementation of a high frequency electrical impedance tomography system,” *Physiol. Meas.*, vol. 25, no. 1, pp. 379–390, Feb. 2004.
- [21] J. W. Lee, T. I. Oh, S. M. Paek, J. S. Lee, and E. J. Woo, “Precision constant current source for electrical impedance tomography,” in *Proc. 25th Annu. IEEE Int. Conf. Eng. Med. Biol. Soc.*, Sep. 2003, pp. 1066–1069.
- [22] S. Hong *et al.*, “A 4.9 m $\Omega$ -sensitivity mobile electrical impedance tomography IC for early breast-cancer detection system,” in *ISSCC Dig. Tech. Papers*, Feb. 2014, pp. 316–317.
- [23] S. Kim, R. F. Yazicioglu, T. Torfs, B. Dilpreet, P. Julien, and C. Van Hoof, “A 2.4  $\mu$ A continuous-time electrode-skin impedance measurement circuit for motion artifact monitoring in ECG acquisition systems,” in *Symp. VLSI Circuits Dig. Tech. Papers*, Jun. 2010, pp. 219–220.
- [24] R. F. Yazicioglu, P. Merken, R. Puers, and C. Van Hoof, “A 60  $\mu$ W 60 nV/ $\sqrt{\text{Hz}}$  readout front-end for portable biopotential acquisition systems,” *IEEE J. Solid-State Circuits*, vol. 42, no. 5, pp. 1100–1110, May 2007.
- [25] R. G. Carvajal *et al.*, “The flipped voltage follower: A useful cell for low-voltage low-power circuit design,” *IEEE Trans. Circuits Syst. I, Reg. Papers*, vol. 52, no. 7, pp. 1276–1291, Jul. 2005.
- [26] H.-Y. Tai, Y.-S. Hu, H.-W. Chen, and H.-S. Chen, “A 0.85 fJ/conversion-step 10b 200 kS/S Subranging SAR ADC in 40 nm CMOS,” *ISSCC Dig. Tech. Papers*, Feb. 2014, pp. 196–197.



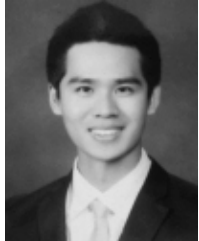
**Minseo Kim** (S'14) received the B.S. degree in semiconductor system engineering, Sung Kyun Kwan University, Seoul, South Korea, in 2014, and the M.S. degree in electrical engineering from the Korea Advanced Institute of Science and Technology, Daejeon, South Korea, in 2016, where he is currently pursuing the Ph.D. degree.

His current research interests include low-power biomedical SoC for wearable healthcare system.



**Jiwon Lee** (S'16) received the B.S. degree in electrical engineering from the Korea Advanced Institute of Science and Technology, Daejeon, South Korea, in 2016, where he is currently pursuing the M.S. degree.

His current research interests include biomedical SoC design, especially focused on low-power signal processors.



**Jae-eun Jang** (S'13) received the B.S. degree in electrical engineering from the Korea Advanced Institute of Science and Technology, Daejeon, South Korea, in 2014, where he is currently pursuing the M.S. degree.

He focused on developing a low-power wireless transceiver and low-power sensor front-end. His current research interest includes low-power transceiver design for body-area-networks and low-power biomedical SoC design.



**Kyoung-Rog Lee** (S'15) received the B.S. degree in electrical engineering from the Korea Advanced Institute of Science and Technology, Daejeon, South Korea, in 2015, where he is currently pursuing the M.S. degree.

His current research interests include low-power biomedical system-on-a-chip (SoC) for wearable healthcare system and body channel communication SoC for low-power communication system.



**Hyunki Kim** (S'13) received the B.S. degree in mathematical sciences and the M.S. degree in electrical engineering from the Korea Advanced Institute of Science and Technology, Daejeon, South Korea, in 2010 and 2015, respectively, where he is currently pursuing the Ph.D. degree.

His current research interests include biomedical SoC design, especially focused on low-power signal processors.



**Kwantae Kim** (S'15) received the B.S. and M.S. degrees in electrical engineering from the Korea Advanced Institute of Science and Technology, Daejeon, South Korea, in 2015 and 2017, respectively, where he is currently pursuing the Ph.D. degree.

His current research interests include low-power bio-medical SoC for wearable healthcare system.



**Jihee Lee** (S'15) received the B.S. degree in electrical engineering from the Korea Advanced Institute of Science and Technology, Daejeon, South Korea, in 2015, where she is currently pursuing the M.S. degree.

Her current research interests include low-power biomedical SoC for wearable healthcare system, energy harvesting, and human body communication SoC for low-power application.



**Yongsu Lee** (S'13-M'16) received the B.S. and M.S. degrees in electrical engineering from the Korea Advanced Institute of Science and Technology (KAIST), Daejeon, South Korea, in 2013 and 2015, respectively, where he is currently pursuing the Ph.D. degree.

His current research interests include low-power biomedical SoC for wearable healthcare system, and human body communication SoC for low-power application.



**Jaehyuck Lee** (S'12) received the B.S. degree in electrical engineering from the Korea Advanced Institute of Science and Technology, Daejeon, South Korea, in 2014, where he is currently pursuing the M.S. degree.

His current research interests include biomedical system design and verification, especially focused on electrical stimulator and biosignal sensor, and body-channel communication for low-power wireless body area network.



**Kyuho Jason Lee** (S'12) received the B.S. and M.S. degrees from the School of Electrical Engineering, KAIST, Daejeon, South Korea, in 2012 and 2014, respectively, where he is currently pursuing the Ph.D. degree.

His current research interests include the development of analog/digital mixed-mode neural network SoC design, object matching processor and its algorithm for computer vision, energy-efficient Network-on-Chip-based SoC design for mobile devices, and intelligent vision processor for advanced driver assistance system.



**Hoi-Jun Yoo** (M'95–SM'04–F'08) received the bachelor's degree from the Electronic Department, Seoul National University, Seoul, South Korea, in 1983 and the M.S. and Ph.D. degrees in electrical engineering from the Korea Advanced Institute of Science and Technology (KAIST), Daejeon, South Korea, in 1985 and 1988, respectively.

Since 1998, he has been the Faculty Member with the Department of Electrical Engineering, KAIST, where he is currently a Full Professor. From 2001 to 2005, he was the Director of the Korean System Integration and IP Authoring Research Center, Seoul, South Korea. In 2007, he founded the System Design Innovation and Application Research Center at KAIST. Since 2010, he has been serving as the General Chair of the Korean Institute of Next Generation Computing, Seoul. He has co-authored *DRAM Design* (Korea: Hongrung, 1996), *High-Performance DRAM* (Korea: Sigma, 1999), *Future Memory: FRAM* (Korea: Sigma, 2000), *Networks On Chips* (Morgan Kaufmann, 2006), *Low-Power NoC for High-Performance SoC Design* (CRC Press, 2008), *Circuits at the Nanoscale* (CRC Press, 2009), *Embedded Memories for Nano-Scale VLSIs* (Springer, 2009), *Mobile 3-D Graphics SoC From Algorithm to Chip* (Wiley, 2010), *Biomedical CMOS ICs* (Springer, 2011), *Embedded Systems* (Wiley, 2012), and *Ultra-Low-Power*

*Short-Range Radios* (Springer, 2015). His current research interests include computer vision SoC, body area networks, and biomedical devices and circuits.

Dr. Yoo was a recipient of the Electronic Industrial Association of Korea Award for his contribution to DRAM technology in 1994, the Hynix Development Award in 1995, the Korea Semiconductor Industry Association Award in 2002, the Best Research of KAIST Award in 2007, the Scientist/Engineer of this month Award from the Ministry of Education, Science and Technology of Korea in 2010, the Best Scholarship Awards of KAIST in 2011, and the co-recipient of ASP-DAC Design Award 2001, Outstanding Design Awards of 2005, 2006, 2007, 2010, 2011, and 2014 A-SSCC, and the Student Design Contest Award of 2007, 2008, 2010, and 2011 DAC/ISSCC. He received the Order of Service Merit from the Ministry of Public Administration and Security of Korea in 2011. He has served as a member of the executive committee of ISSCC, the Symposium on VLSI, and A-SSCC, and the TPC Chair of the A-SSCC 2008 and ISWC 2010, the IEEE Distinguished Lecturer from 2010 to 2011, the Far East Chair of ISSCC 2011 to 2012, the Technology Direction Sub-Committee Chair of ISSCC in 2013, the TPC Vice Chair of ISSCC in 2014, and the TPC Chair of ISSCC in 2015. From 2003 to 2005, he was the full-time Advisor to the Minister of Korea, Ministry of Information and Communication, and National Project Manager of SoC and Computer.